UKAEA-CCFE-PR(21)04

M. Knolker, T. Osborne, E. Belli, S. Henderson, A. Kirk, L. Kogan, S. Saarelma, P. B. Snyder

Pedestal Stability Analysis on MAST in preparation for MAST-U

Pedestal Stability Analysis on MAST in preparation for MAST-U

M. Knolker, T. Osborne, E. Belli, S. Henderson, A. Kirk, L. Kogan,

S. Saarelma, P. B. Snyder

Pedestal Stability Analysis on MAST in preparation for MAST-U

M. Knolker[a*], T. Osborne[a], E. Belli[a], S. Henderson[b], A. Kirk[b], L. Kogan[b], S. Saarelma[a], P. B. Snyder[a]

[a] *General Atomics, San Diego, CA 92186-5608, USA*
[b] *United Kingdom Energy Authority, Oxford, UK*

* corresponding author, email: knolkerm@fusion.gat.com

Abstract

In preparation for the upcoming MAST-U campaign, pedestal stability of spherical tokamaks is revisited by investigating standard H-mode discharges on MAST. As a step beyond previous studies, both ion and electron profiles are used for obtaining equilibria and a diverse set of pedestals is evaluated. Stability analysis with the ELITE and CGYRO codes shows that MAST pedestals are constrained by medium range peeling-ballooning and kinetic ballooning modes, with most unstable modes ranging from n=25 to n=45. In discharges with a steep q profile at the edge a larger number of poloidal harmonics is excited for each toroidal mode. A comparison with discharges on DIII-D with matched shape and similar non-dimensional parameters indicates that the increased shear due to lower aspect ratio stabilizes peeling mode drive.

1. Introduction and state of the question

Spherical tokamaks are characterized by their small aspect ratio $A = \frac{R}{a} \sim 1.2 - 2.0$, with a the minor and R the major radius, resulting in access to higher values of elongation κ=1.5-3, edge safety factor q_{95}=4-20 and normalized beta $\beta_N = 3 - 6$ compared to standard tokamaks [1–3]. The attractiveness and promise of spherical tokamaks consists of achieving higher normalized plasma parameters than standard aspect ratio tokamaks with the same volume, thus reducing overall costs for potential future fusion power plants [4].

In general, a proven strategy for raising tokamak confinement is optimizing the H-mode pedestal [5], since it provides boundary conditions for both core and divertor region. The idea is readily explained: If the transport in the plasma core is limited by the onset of ion temperature gradient modes resulting in a critical gradient and so-called profile stiffness, then a higher pedestal will elevate the pressure profile in the core in proportion with the pedestal height, leading to a predicted scaling of fusion power with the square of pedestal pressure [6]. Hence, understanding and optimizing pedestal stability is vital in all tokamaks.

As with moderate aspect ratio tokamaks, the pedestals of spherical tokamaks in standard H-modes are limited by the onset of edge localized modes, repetitive partial collapses of the edge transport barrier, leading to transient confinement degradation and expelling of particles and energy [7,8]. Of particular interest is the type-I or giant ELM [7], since this type is ubiquitous in the standard H-mode scenario, the regime foreseen for ITER and future reactors. The phenomenology of type-I triggering giant ELMs is rather well explained by the peeling ballooning model, identifying current and pressure driven instabilities and their interplay as underlying cause [9].

In previous work, the type-I ELMy plasmas on MAST [10] was shown to reach the high n (n=35-50) peeling-ballooning mode stability limit at the end of the ELM cycle [11–13], whereas in work on NSTX [14], a comparable spherical tokamak, low n peeling-ballooning modes were identified as the dominant instability [15–17]. Understanding pedestal stability of spherical tokamaks is important for extrapolation towards future machines as MAST-U [18] or power plants based on this concept since the response of the pedestal highly varies depending on the nature of its limitation: For instance, low n peeling-ballooning-modes are dominated by the peeling character (driven by the edge current gradient, resulting primarily from bootstrap current) and the pedestals limited by them tend to respond by increasing height to a density rise since the associated higher collisionality reduces the bootstrap current, whereas ballooning dominated pedestals react negatively to bootstrap current reduction, as this increases magnetic shear.

Hence, the scope of this paper is undertaking pedestal stability analysis on MAST standard H-modes with type I ELMs on a diverse set of pedestals (section 2 and 3). Moreover, a broadening of the understanding by comparing results to matched discharges of the DIII-D tokamak[19] (section 4), and ultimately extrapolating to MAST-U (sections 5 and 6).

2. Experimental setup and diagnostics

To ensure generality in the edge stability analysis on MAST, wide ranges of relevant parameters, such as pedestal temperature and collisionality, need to be covered. Hence, a discharge selection was made from several MAST campaigns spanning half a decade of research. The on-axis toroidal magnetic field in the dataset ranges from B_T= 0.4-0.5 T, plasma current is I_P= 0.5-0.9 MA and injected neutral beam powers are P_{NBI}= 1.5-3.5 MW. The plasma shapes are in single and double null configuration, spanning average triangularities of δ =0.35-0.5 and elongations κ=1.7-2.0 Electron profiles on MAST are measured with a Thomson scattering diagnostic consisting of two systems [20,21], providing a spatial resolution down to 5 mm. Characteristics of ions are evaluated with a charge exchange recombination system [22]. Furthermore, neutron rates are monitored with a system of several detectors [23] and used to constrain the anomalous diffusion rates necessary to determine the fast ion profile, as explained in the later segments of this section.
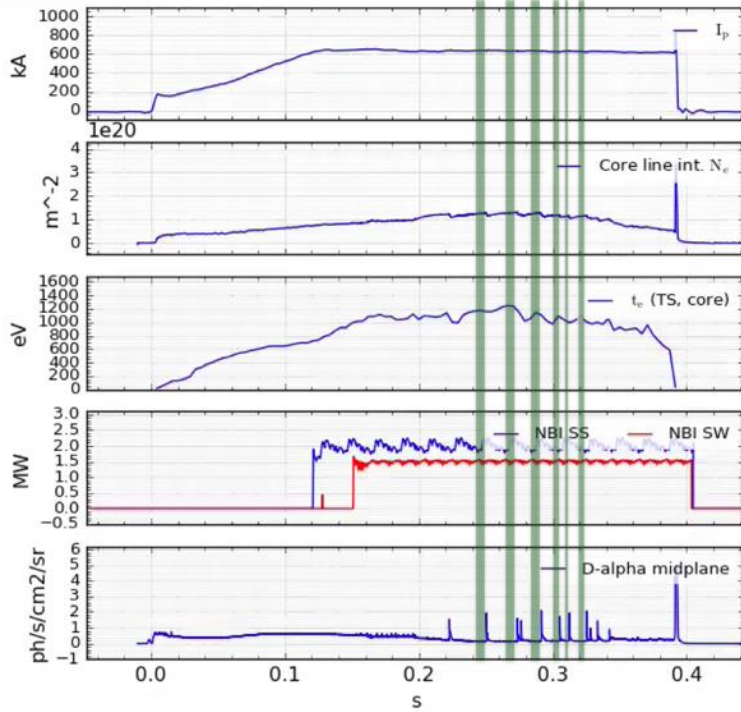
Figure 1 Discharge trajectory of a type I standard ELM H-mode on MAST a) plasma current b) core density c) core electron temperature d) NBI heating power by southwest (blue) and south system (red) e) D-α recycling near the midplane. The 80-99 % time intervals prior to type I ELMs are shaded in green.

A typical discharge trajectory is shown in figure 1. Following a ramp in the plasma current (a), core density (b) and temperature (c) are rising, supported by the injection of neutral beam power (d) from both the south and southwest system. Heating power is kept constant in these discharges, so that the pedestal conditions outside of the ELM cycle remain relatively stationary. The LH-transition occurs at 0.15 s and is initiated with type III dithering ELMs, visible in the D-α recycling trace (e). Once a sufficiently high density is reached, the plasma can access the type I ELM regime. The green shaded areas mark the 80-99 % ELM intervals, which are used for obtaining profiles for the pedestal stability analysis.

A representative set of profiles for this discharge is shown in figure 2. In general, the raw measurement data is collected over a time window of 80 ms to 200 ms (here from 0.25 s to 0.33 s) and then conditionally averaged over the 80-99 % ELM interval. Typically, the core plasma is fit using polynomials and the edge profiles with a spline or the well-established hyperbolic tangent fit [24]. As can be seen, the electron density n_e is monotonically decreasing in the core but has a small rise in the core-edge blending region next to the step gradient edge (a). Since there is no carbon impurity density measurement n_C, the profile (e) has to be inferred assuming an effective charge, typically in the range of Z_{eff}=1.5-2. The impact of this choice for stability is evaluated in section 3.4 of this paper. Since neutral beam injection is the dominant heating source in these
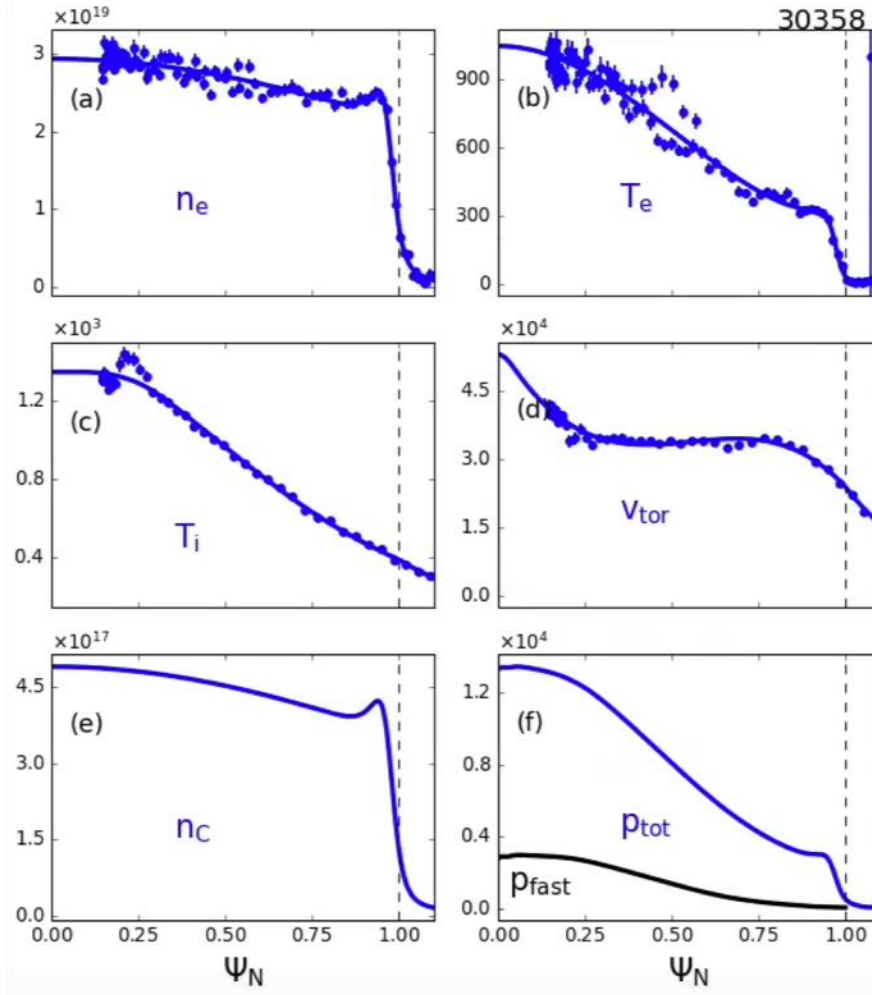
3

Figure 2 Obtained profiles from conditionally averaging over the 80-99 % ELM phase; a) electron density and b) temperature, c) ion temperature and d) toroidal rotation as measured by CER, e) calculated carbon impurity density f) fast ion pressure (black) and total pressure (blue)

discharges, the ion temperature T_i (c), strongly exceeds the electron temperature T_e in the edge region (b). A toroidal rotation measurement of the carbon ions v_{tor} (d) is used to calculate the radial electric field E_R. Due to the lack of a poloidal ion velocity measurement, v_{pol}=0 will be assumed for the E_R calculation. Fast ion profiles are generated using TRANSP[25,26]. Significant anomalous diffusion with a coefficient on the order of 2.0-4.0 $\frac{m^2}{s}$ is required to match the neutron rates with experimental values. The TRANSP calculated neutron rate is mainly based on beam-target collisions with a negligible fraction of thermal fusion neutrons and beam-beam collisions. The fast ion and total pressure profiles are shown in (f). The latter resembles the typical standard H-mode tokamak profile features, namely a pedestal upon which the plasma core resides.

There are two important alignment choices that have to be made for the profile fitting:

- Symmetrization: Due to the strong variation of the major radius between high and low field sides in spherical tokamaks the spacing between flux surfaces also varies strongly. This can make the high and low field side measurements difficult to align. Hence an algorithm-based optimization is undertaken, aiming to minimize residuals in the overlaying fits of high and low field side by orienting and shifting measurement points on the respective flux surfaces.
- Finding the appropriate separatrix temperature $T_{e,sep}$: Based on heating power, $T_{e,sep}$ is chosen between 35-50 eV (resulting in an ion separatrix temperature ranging between 120-180 eV). A bad choice of separatrix temperature can lead to a bad alignment between magnetics and Thomson profiles and result in a non-convergence of the Grad-Shafranov equation computed by EFIT[27], in which case the fitting process is iterated with a different temperature choice.

In a final step towards the equilibrium, the thermal and fast ion profiles are mapped on magnetic surfaces to generate kineticEFITs. A kinetic EFIT is an axisymmetric solution to the toroidal equilibrium as described by the Grad-Shafranov equation and constrained by magnetic probe and flux loop data, and by the plasma pressure profile, including the correction for the fast ion pressure and inclusion of the Sauter model for the pedestal bootstrap current [27,28]. For this purpose, a modified version of EFIT, EFIT++ is used, which is adapted to MAST.
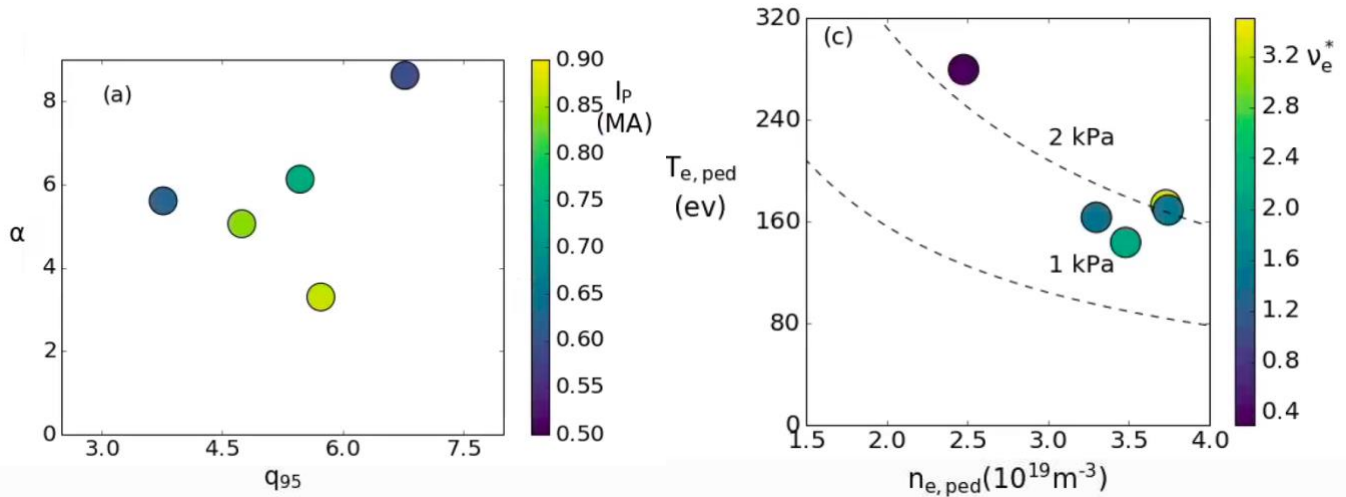

Figure 3 Overview of kinetic equilibria in different parameter spaces a) Dependence of maximum of normalized pedestal pressure gradient on safety factor and plasma current b) pedestal temperature and density with their respective collisionality

Figure 3 visualizes the range of selected parameters covered by experimental equilibria reconstructed as described above. The normalized pressure gradient α is defined as [29]

$$\alpha = \frac{\mu_0}{2\pi^2} \frac{\partial V}{\partial \psi} \left(\frac{V}{2\pi^2 R}\right)^{\frac{1}{2}} \frac{\partial p}{\partial \psi}$$

Here, μ_0 is the vacuum permeability, V is the volume enclosed by a flux surface with the poloidal flux ψ, R is the plasma major radius and p the pressure. In general, α is growing with the safety factor (and smaller plasma currents) (Figure 3a), which is expected based on simplified derivations for circular plasmas if the pressure gradient is kept fixed [30]. The pedestal pressure range covered ranges from 1.5-2.2 kPa (Figure 3b) with pedestal temperatures up to about 300 eV and pedestal electron collisionalities ν_e^* between 0.3-3.2. Collisionality is a measure for how often electrons at the plasma edge collide. In general, it is compared at the pedestal top and calculated via [28]

$$\nu_e^* = 6.921 \cdot 10^{-18} \cdot q_{95} \cdot R_{max} \cdot n_{e,ped} \frac{\left(1 + 30 \cdot \frac{n_{C,ped}}{n_{e,ped}}\right) \cdot \left(31.3 - \ln\frac{n_{e,ped}^{0.5}}{T_{e,ped}}\right)}{T_{e,ped}^2 \cdot \left(\frac{a}{R_{Surf}}\right)^{1.5}}$$

where R_{Surf} is the major radius of the center of the outermost closed flux surface, and all quantities with subscript ped refer to the respective value at the pedestal top. Note that in the investigated MAST dataset, a large span of ν is covered for high pedestal pressure, in order to evaluate the influence of collisionality and improve extrapolation to MAST-U.

To summarize, this section has described the process for obtaining profiles and equilibria on MAST and building a database, demonstrating its generality and repeatability with the caveats of several necessary choices (separatrix temperature, LFS/HFS alignment). Unique features of the low aspect ratio machine that could influence pedestal stability are the high safety factor and resulting large normalized pressure gradient. The discharges used for the comparison with DIII-D and their experimental setup are described in section 4, since the majority of this paper is based on MAST data.

3. Pedestal stability analysis

3.1 Physics of edge modes in low aspect ratio tokamaks

Prior to conducting peeling ballooning stability analysis on the generated equilibria, the primary physic effects of low aspect ratio and high safety factor have to be considered to adjust the setup of the stability codes. This mainly concerns the number of poloidal modes excited for each toroidal mode number. Due to the high safety factor and magnetic shear, resonant surfaces are closer to each other in the edge region, facilitating coupling of a large number of poloidal modes.   In addition, low aspect ratio leads to stronger coupling of poloidal modes (at infinite aspect ratio, poloidal modes are uncoupled). Due to the combination of these effects, MHD stability codes such as ELITE [9,9a], which use a poloidal mode decomposition, require substantially larger numbers of poloidal modes to reach convergence than in typical cases at moderate aspect ratio. To illustrate the contrast between MAST and DIII-D, growth rates in dependence of poloidal window size are visualized for an n=35 mode on DIII-D and MAST (figure 4). One can see that the growth rate reaches saturation for a poloidal mode window of 15 poloidal modes on DIII-D (blue), whereas on MAST a poloidal window with up to 50 modes can be necessary for convergence.
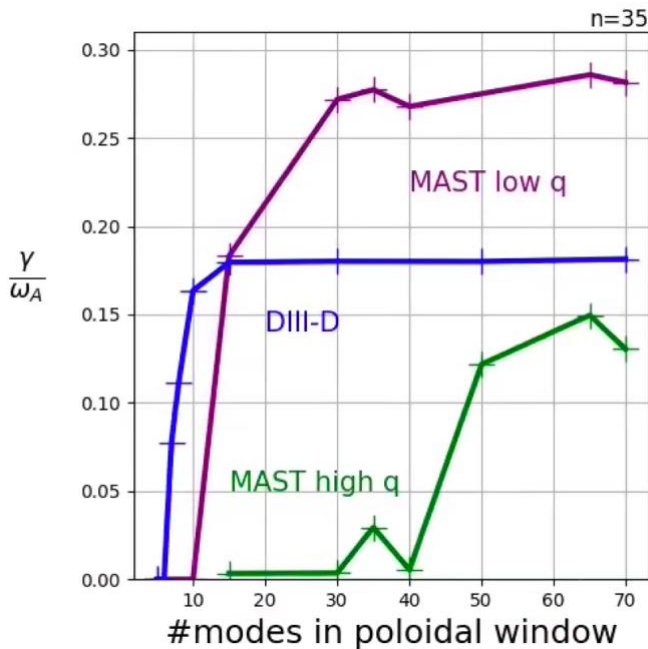

Figure 4 Growth rates in dependence of poloidal mode number window size for an n=35 peeling-ballooning mode on a matched DIII-D discharges with q_{95}=2.8 (blue) and two MAST equilibria with q_{95}=3.8 (purple) and q_{95}=6.8 (green)

Hence, the input parameters of ELITE [9] need to be adjusted accordingly. To resolve the fine structure of high n ballooning modes numerically, the mesh has to be refined to a grid with 2049 points instead of 513 (EFIT grid 513x513 instead of 129x129). This comes at the cost of higher memory use and computational time required by ELITE, up to 30 times more computational time than a standard tokamak calculation at the same toroidal mode number.
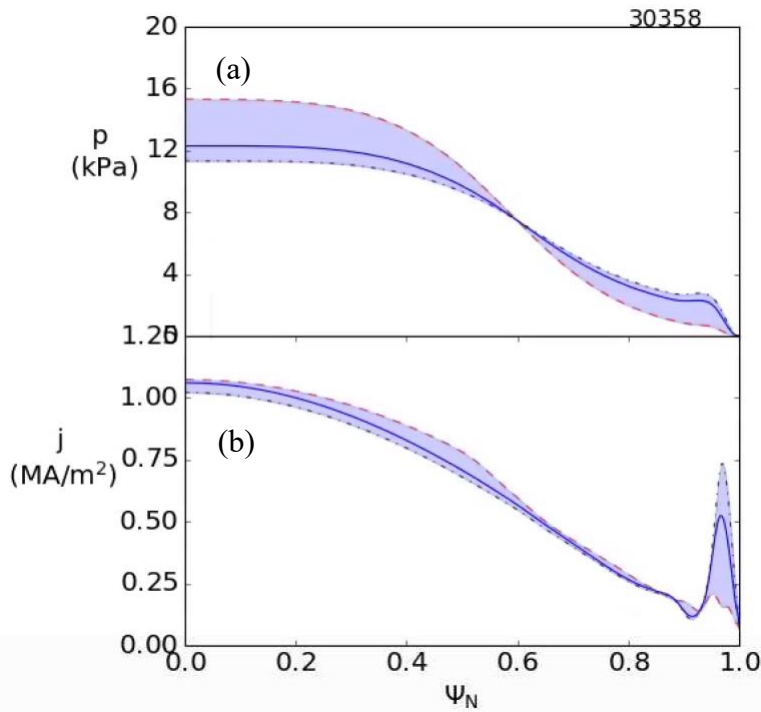

Figure 5 Variation of plasma pedestal pressure and edge current with VARYPED on MAST discharge 30358. Original equilibrium in blue with envelope function showing the extent of the scan

For the illumination of the pedestal stability limitation, a set of equilibria is generated for each discharge using the VARYPED code in fixed boundary mode (figure 5). The original equilibrium is indicated by the blue line and the envelope function symbolizes the range of equilibria with higher and lower pedestal pressure (a) and edge currents (b). Both pressure and current are varied self-consistently conserving the overall beta (a) and total current, and respectively safety factor at the separatrix (b). In a typical setup both normalized edge pressure gradient and current are varied from about a third to twice their value.

An example of a resulting MAST peeling ballooning diagram for a high safety factor, high collisionality DND discharge 29795 (q_{95}=6.8, v_e^*=3.4) is shown in figure 6a. The x-axis represents the normalized pressure gradient α, the y-axis the ratio of the sum of the edge current density maximum and the current density at the separatrix to the average current density. Within the

scanned region, the peeling boundary is far away from the operational point. Since the pedestal electron collisionality ν_e^* is rather high in this case and higher collisionality leads to a suppression of the bootstrap current, one would expect a stabilization of peeling modes. Note that the collisionality is on the lower bound of the experimental value range, since ν_e^* scales linearly with Z_{eff}, which was chosen as $Z_{eff}=1.5$, so on the lower end of the parameter range.
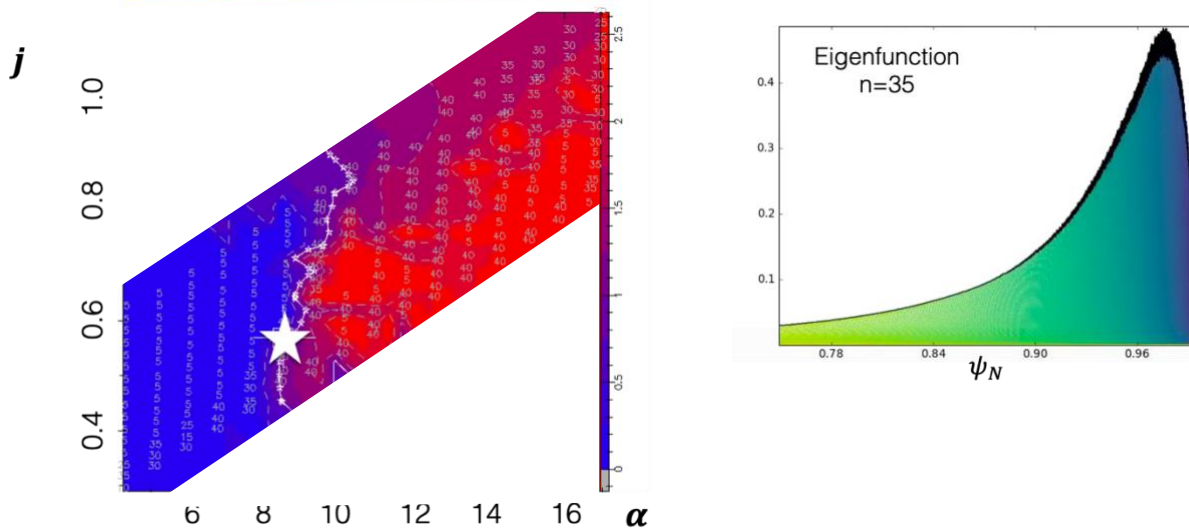

Figure 6 a) Peeling ballooning diagram of discharge 29795 b) Radial eigenfunction of n=35 PB mode

The most unstable mode is in the n=35-40 range and the n=35 eigenfunction is visualized in figure 6b. It peaks around $\psi_N = 0.97$. The results presented above are representative for the array of analyzed equilibria and also agree with results from previous stability analysis on MAST based on electron profile measurements only[11,13].

3.2 Kinetic Effects in low aspect ratio tokamaks

Since ELITE is a linear MHD code, the validity of MHD assumptions for MAST pedestals has to be verified. This primarily concerns high safety factor equilibria at low magnetic field, for which the ion gyro radius and the poloidal mode width can become of similar order. For instance, for the n=35 case above (figure 6), the calculated poloidal mode width and the ion gyro radius are both approximately 0.02 m. Consequently, kinetic effects have to be considered. Using the local electromagnetic gyrokinetic CGYRO code [31,32], the mode growth of n=35 is evaluated for various locations in the pedestal (figure 7).
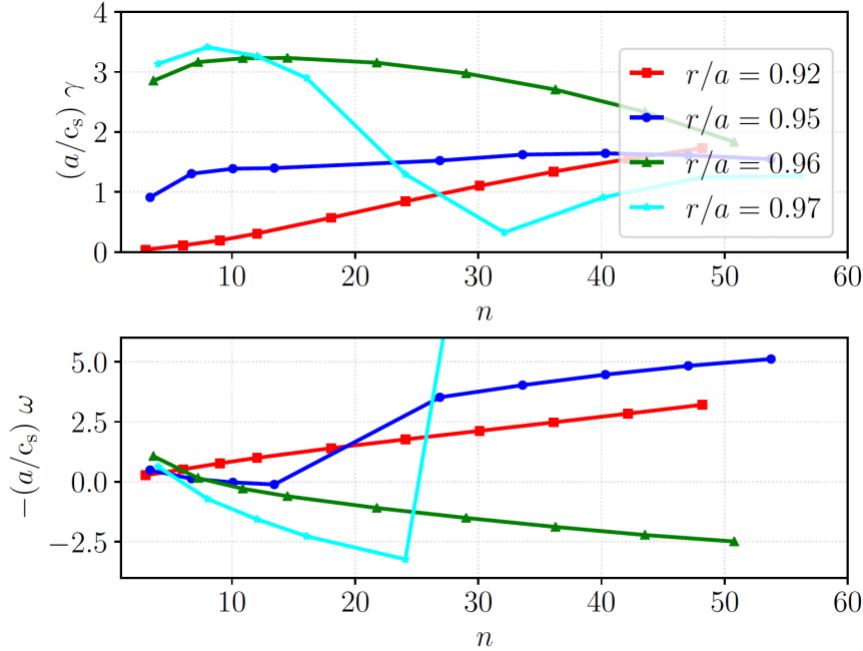
Figure 7 CGRYO analysis of discharge 29795: Growth rates of modes rotating in ion and electron direction for various locations in the pedestal region.

With regards to sign convention, modes rotating in the ion direction are positive and modes rotating in the electron direction negative. The analysis shows that in the region of interest (r/a=0.95-0.96) the positively rotating mode, is dominant up to the high n spectrum (n=40). A scan of the electron beta (not shown here) reveals that a marginal increase in beta would strongly drive the mode, which hence can be identified as a kinetic ballooning mode. The mode rotating in the electron direction that has the highest growth rate for high n modes above 40, can be identified as a micro-tearing mode. Note that the growth rate of the kinetic ballooning mode decreases only marginally towards the low n range, since CGYRO is a local code and hence cannot take the actual pedestal width into account. Doing so would show that the steep gradient region is too narrow for a broad low n mode, as calculated by ELITE. The analysis with CGYRO confirms the dominance of a ballooning mode and shows that -while there is stabilization due to finite Larmor radius (FLR) and other kinetic effects – medium to high n ballooning modes are strongly unstable, and would be expected to drive large transport and constrain the pedestal pressure gradient, and therefore the pedestal height at a given width.. This finding is in agreement with previous analysis [12,33], where the formation of the pedestal throughout the ELM cycle on MAST was described as a competition process between a kinetic ballooning mode in the step gradient region and an MTM localized near the pedestal top. Since the kinetic corrections do not alter the results significantly, the following analysis on the full range of discharges is conducted using ELITE.

3.3 Overview of dataset

Selected peeling ballooning maps as calculated by ELITE for various equilibria introduced in figure 3, are shown in figure 8. All equilibria are medium to high n ballooning limited with critical mode numbers in the range of 35-50. The biggest difference between the equilibria is the proximity to the peeling boundary. Due to the medium to high range of collisionality, most cases are similar in appearance as discharge 24763 (shown in Figure 8 a), where a doubling of the normalized edge current would be necessary to get to the peeling limit. In contrast, the lower single null case with low collisionality (Figure 8 b) only allows about a 30 % increase in j_n.
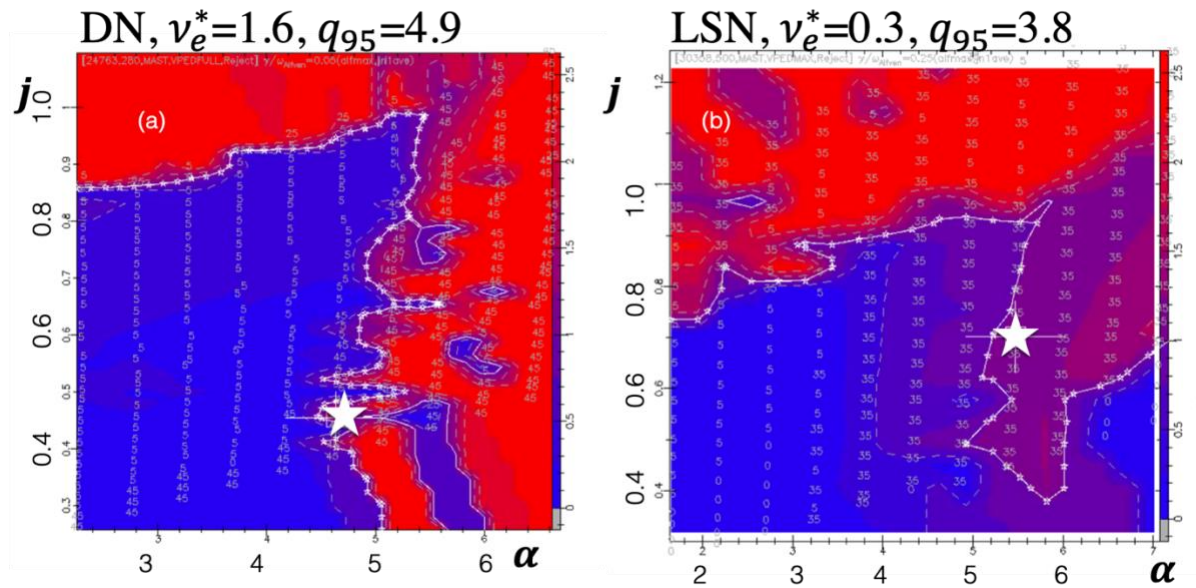

Figure 8 Pedestal stability analysis on selected MAST equilibria a) Double null shape with medium collisionality and safety factor b) low collisionality, and low safety factor equilibrium closer to the peeling boundary

With regards to the mode structure, the limits of pedestal stability are hence dominated by a low n mode (usually n=5) on the peeling side and a medium to high n mode (as n=40) on the ballooning side. When comparing the q-profiles near the peeling limited region for these discharges, the peeling limit coincides with q-profile becoming flat or reversed near the edge due to the large size of the bootstrap current. Mode numbers in between (as n=10-30) are gradually limiting the available space on the ballooning side but smaller in growth rates then the dominant high n mode.

3.4 Influence of rotation and effective charge

Following the stability analysis, the influence of the choice of effective charge and rotation will be analyzed. For this purpose, a low safety factor equilibrium is chosen and analyzed assuming an effective charge of a) $Z_{eff} = 1.5$, b) $Z_{eff} = 2.5$ and c) $Z_{eff} = 2.0$ and $T_e = T_i$ (figure 9). One

can see that both the higher effective charge and the sole electron profile-based analysis reduce the resulting pedestal pressure (Figure 9a). This is understandable, since the ion temperature is hotter than the electron temperature at the edge, and higher effective charge at a given electron density
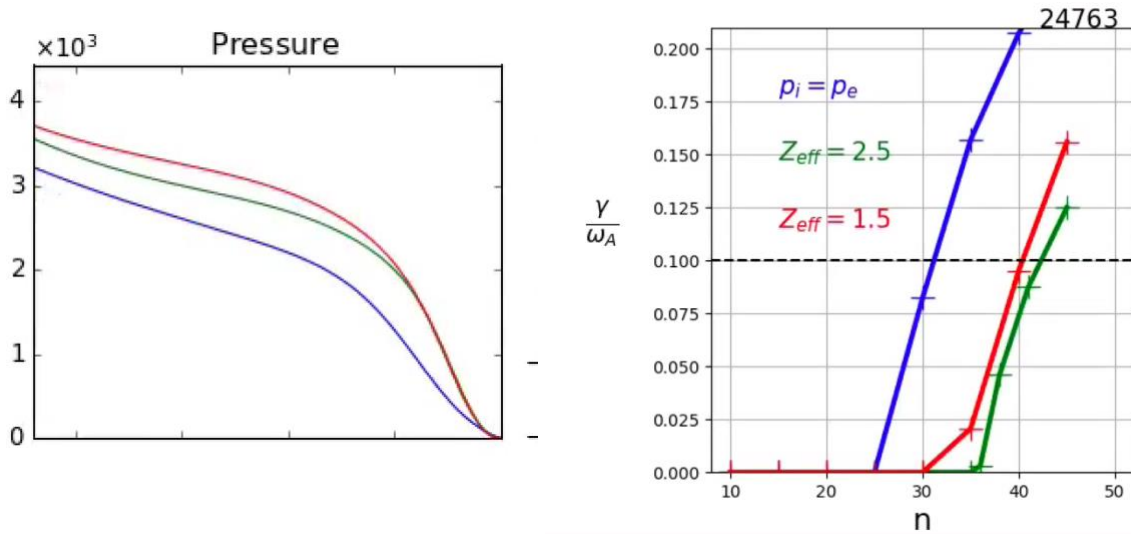

Figure 9 Impact of effective charge on pedestal stability on discharge 24764=3 a) Total pressure for Zeff=1.5 (red), Zeff=2.5 (green) and similar ion-electron pressure (blue) b) Growth rates in dependence of mode number

causes more fuel dilution and lower pressure. While the qualitative result of medium to high n mode ballooning limited pedestals is conserved, the most unstable mode number is affected and increasing with effective charge but decreasing with lower overall pressure profile (figure 9b).

This section has shown that MAST pedestals are limited by medium to high n peeling ballooning modes and their kinetic equivalent. Effective charge plays a minor role for pedestal stability.
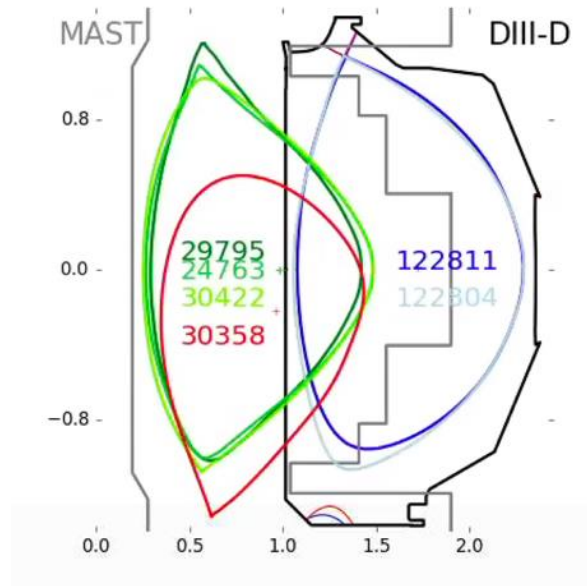
4. Comparison to DIII-D

Figure 10 Shape comparison of matched MAST (green) and DIII-D (blue) discharges. Added MAST discharge for study of low collisionality effects (red).

In order to evaluate the influence of aspect ratio on pedestal stability, DIII-D discharges with matched MAST shapes from a multi machine pedestal scaling study [34] were selected with the goal of matching pedestal parameters (see figure 10). A MAST discharge (30358) with different shape, but very low collisionality is added to provide additional insights. An overview of the selected discharges is shown in table 1.

shot	MAST (R/a)=1.3				DIII-D (R/a)=2.9	
	29795	30422	24763	30358	122804	122811
B_T [T]	0.4	0.4	0.5	0.4	0.5	0.8
I_P [MA]	0.6	0.7	0.8	0.6	0.6	0.8
P_{NBI} [MW]	3.5	3.5	3.5	3.5	1.5	1.2
κ	2.0	1.7	1.7	1.7	1.7	1.7
δ (δ_{min})	0.5 (0.4)	0.5 (0.5)	0.5 (0.5)	0.4 (0.2)	0.5 (0.5)	0.5 (0.4)
q_{95}	6.8	5.3	4.9	3.8	2.4	2.8
β_N	4.2	3	3.3	3.0	2.2	1.9
p_{ped} [kPa]	1.6	1.8	2.2	2.8	2.8	2.5

$T_{e,ped}$ [keV]	0.16	0.17	0.17	0.28	0.24	0.23
ν_e^*	3.4	2.2	1.6	0.4	4.0	4.1
Z_{eff}	1.5	1.6	1.6	1.5	3.8	3.1
α	8.6	6.1	5.1	5.7	3.7	4.2
β_{pol}	0.19	0.14	0.13	0.23	0.35	0.18
f_{bs} [%]	22	16	12	10	10	13

Table 1 Overview of selected MAST and DIII-D discharges

Within the matched shape MAST discharges (29795, 30422, 24763), a span from high to low safety factor and normalized pressure gradient is covered. Since the safety factor reduction is reached through a raise of the plasma current, the pedestal density increases with lower safety factor, allowing higher pedestal pressure. The discharge with the highest q_{95} and lowest plasma current consequently has the lowest pedestal pressure but highest normalized β_N. Since the bootstrap current fraction scales with the poloidal beta $f_{bs} \sim \frac{a}{R} \beta_{pol}$ [28] and the poloidal beta increases with β_N and κ [35]

$$\beta \cdot \beta_{pol} = 25 \frac{1 + \kappa^2}{2} \left(\frac{\beta_N}{100} \right)^2$$

discharge 29795 has the highest bootstrap current fraction of 22 % within the type I ELM dataset. Despite of its high β_{pol} and low collisionality, discharge 30358 comes with the smallest bootstrap current fraction due the low safety factor.

For the DIII-D matched cases, both have an elongation of 1.7 and an average triangularity of 0.5, but in the case of 122811 this is achieved by an upper triangularity of 0.6 and a lower triangularity of 0.4, whereas on 122804 this is achieved in a symmetric way. It has been shown elsewhere that the lower value of both triangularities is a better indicator for pedestal behavior than the mean [36]. The resulting peeling ballooning stability diagram for the DIII-D discharges 122811 and 122804 are shown in figure 11. The most unstable mode in both cases is n=40 with a clear ballooning limited plasma. Due to the higher pedestal and lower collisionality, the normalized edge gradient is higher for the 122804 case.
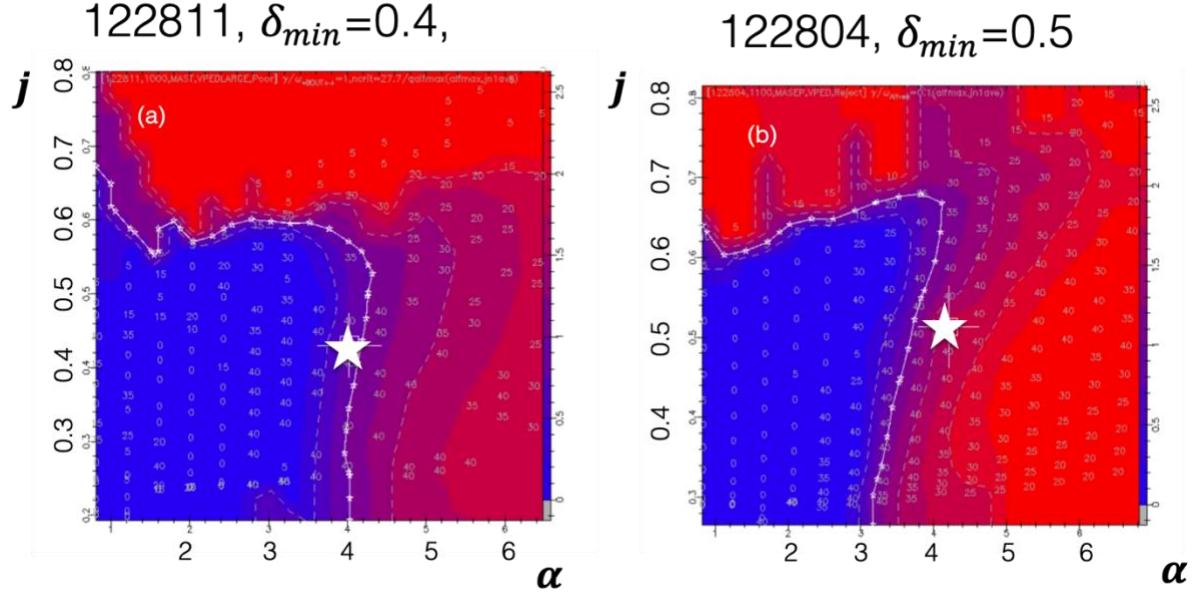
Figure 11 Pedestal Stability analysis on matched DIII-D discharges with a) asymmetric and b) symmetric triangularity

Compared to the matched shape MAST discharges, the noticeable differences for matched plasma shapes emerge from the lower safety factors on DIII-D (due to the higher aspect ratio), and higher pedestal temperature, despite reduced heating power (see table 1). The higher pedestal temperature explains why DIII-D discharges have similar collisionality despite the higher effective charge. For matched poloidal betas, the bootstrap current fraction on DIII-D is smaller than on MAST.

In direct comparison of pedestal stability results (figures 11 and 6/8), one can see that DIII-D discharges are closer to the peeling limit. Only the MAST case with very low collisionality (30358) gets similar proximity to the peeling limit as the DIII-D cases. This might be surprising given the facts that a) the bootstrap current fractions are higher on the MAST discharges and more current drive destabilizes peeling modes and b) the smaller plasma area on the low field side, which is the bad curvature area is expected to stabilize ballooning modes.

However, as shown in figure 12, in the matched shapes and collisionality discharges, the shear s, is higher on MAST discharges for similar pedestal conditions, which affects peeling stability. Stability criteria for peeling modes have been defined several times [37,38], and to understand the impact of shear, it is intuitive to follow [9,39] and to consider the stability criterion for a simplified cylindrical torus [40]

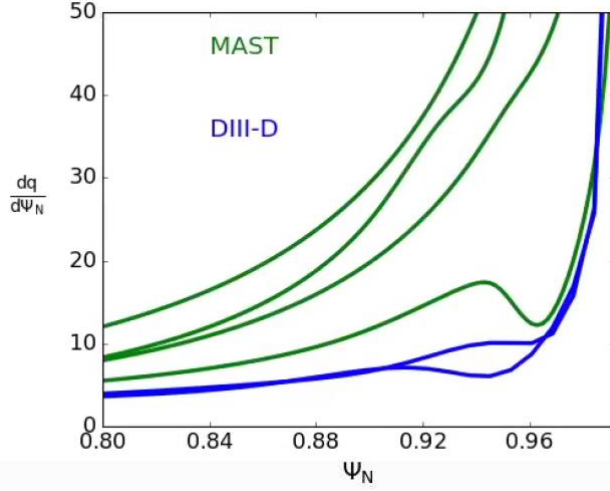$$\sqrt{1 - D_M} > 1 + \frac{1}{\pi q'} \oint \frac{j_\parallel B}{R^2 B_p^3} dl$$

Figure 12 Safety factor gradient as measure for shear for DIII-D (blue) and MAST (green) equilibria used in the comparison study.

where $q' = \frac{dq}{d\psi}$, B_p the poloidal field strength and DM is the Mercier coefficient [41]. The integration is executed along a magnetic field line. Assuming the left side is relatively constant, the equation conveys that a larger safety factor gradient and poloidal field strength relative to the total field will lead to larger tolerable parallel currents in the integral on the right-hand side and stabilize peeling drive. Note that even with a reduction of collisionality to 0.3 and a correlated increase in bootstrap current density at the edge, the discharges are still closer to the ballooning boundary and their relative distance to the peeling boundary matches equals approximately the stability result of high collisionality DIII-D discharges. The shear relative to the pressure gradient is so high that an infinite n ballooning analysis with BALOO [35] predicts no access to second stability in agreement with previous studies [12]. Discharges on DIII-D in the low range of collisionality ($v_e^* < 0.3$) are typically limited by low n peeling ballooning modes and localized in the nose of the peeling ballooning diagram or on the peeling side [42]. Hence, the different aspect ratio does not only affect the shape of the peeling ballooning boundary, but for lower collisionality cases shift the most dominant mode number towards the higher, more ballooning dominated range.

Consequently, the increased shear due to the spherical architecture is the key player for understanding pedestal stability on MAST and spherical tokamaks. Since $q_{95} \sim \frac{a}{R}$, spherical tokamaks have higher safety factors and shear for a given plasma current than standard aspect ratio machines. This improves low-n-peeling mode stability and makes medium to hign n peeling ballooning modes to the limiting edge stability on MAST.

As can be seen in figure 13, showing the radial and poloidal width of the Eigenfuctions, the aspect ratio does not significantly affect the spatial extent of the peeling balloning modes. In both cases, the mode is spread on the low field side and most present in the regions of larger curvature.
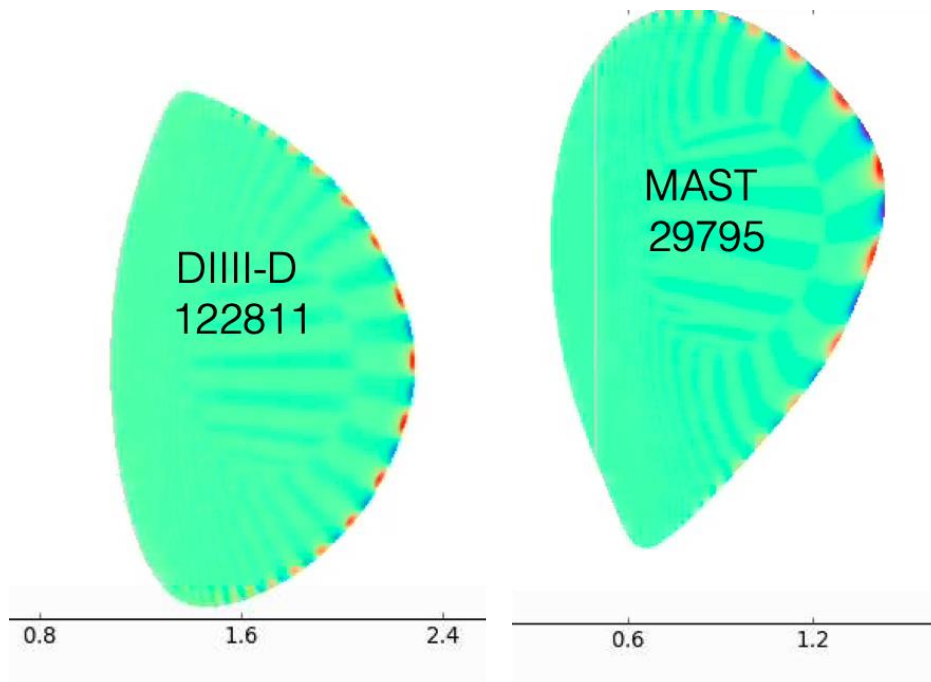
Figure 13 Comparison of radial and poloidal extent of n=35 peeling ballooning mode on DIII-D and MAST.

To conclude, in a direct comparison of pedestal stability between spherical and standard tokamaks, the different aspect ratio and safety factor, lead to an increase of shear in spherical tokamaks stabilizing peeling modes. For determining the most unstable mode number the conclusion must be that aspect ratio is not a dominant factor in determining pedestal stability of type I ELMy H-mode plasmas. Other, more local conditions as the effective charge, collisionality or beta are dominating.

5. Discussion of Results and Implications for MAST-U

Over a wide range of pedestal parameter, MAST plasmas have been shown to be ballooning limited in agreement with previous studies. The investigated discharges match lie within a 20 % error bar of the predicted scaling by the EPED1.6 model [43] that calculates a dependence of the pedestal width on the poloidal pedestal beta with a coefficient of 0.11 using the ballooning critical pedestal technique (figure 14a). For the DIII-D cases the results of the EPED1 model with a scaling of 0.076 are shown within a 25% error bar of the prediction. The EPED model assumes that pedestals are constrained by a local kinetic ballooning mode and a global peeling ballooning mode, delivering two equations for the pedestal width and pressure.
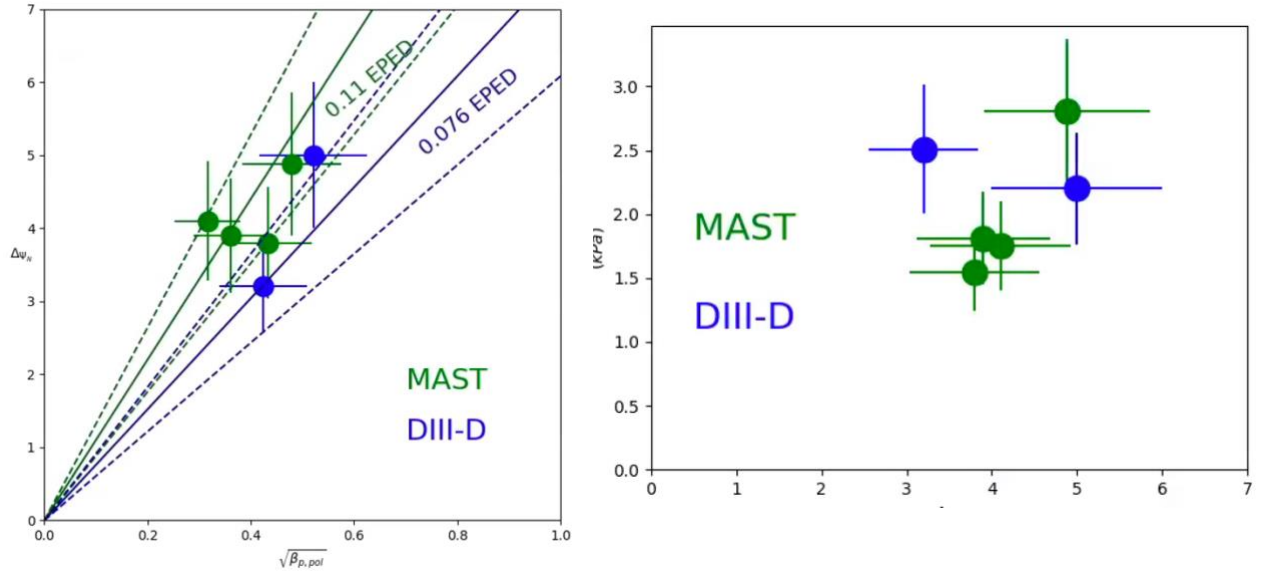

Figure 14 Pedestal width and height of MAST and DIII-D a) pedestal width in dependence of the square root of poloidal beta with the EPED1 (blue) and EPED1.6 (green) model scaling b) dependence of pedestal width on height of selected equilibria.

For similar width the achieved pedestal pressure is higher on DIII-D (figure 14 b). In order to extrapolate to MAST-U a simple approach (assuming among others similar beta values), yields $p_{ped} \sim I_p B_T$. The expected values are listed in table 2 for both MAST-U phases

	MAST	MAST-U (initial)	MAST-U(final)
B_T [T]	0.5	0.6	0.75
I_p [MA]	1.3	1.0	2.0
δ	0.45	0.45	0.5
P_{NBI} [MW]	3.8	3.5	5
$t_{discharge}$ [s]	0.6	2	5
p_{ped} [kPa]	2.2	3.0	7.5

Table 2 Comparison of MAST and MAST-U operational parameter in various stages

6. Summary

Pedestal stability on the low aspect ratio tokamak MAST has been revisited for type I ELM scenarios. Using both experimental ion and electron profiles, kinetic EFITs were reconstructed and investigated for their stability. The following findings were made:

- Over a large pedestal temperature range from 100-300 eV and a collisionality range from 0.3-3.0 MAST equilibria are constrained by high n peeling-ballooning modes with a critical mode number of n=25-45 as shown by the ELITE code
- Kinetic effects as FLR stabilization reduce the growth rate of the modes only marginally as calculated by CGYRO confirming the MHD result
- The error of using ion instead of electron profiles or varying effective charge is rather small and does not affect the qualitative outcome
- Plasmas with matched shape on DIII-D show that for similar pedestal conditions the additional shear on MAST provided by the spherical architecture stabilizes peeling modes and increases ballooning drive

Future work will comprise of applying the fitting routines to NSTX and comparing stability results to previous work. Additionally, DIII-D discharges in MAST shape with lower collisionality could provide more insights into the influence of aspect ratio in the lower collisionality range.

Acknowledgements

Data availability statement

Raw data were generated at the DIII-D national fusion facility. Derived data supporting the findings of this study are available from the corresponding author upon reasonable request.

References

[1]   Peng Y K M 2000 The physics of spherical torus plasmas *Phys. Plasmas*

[2]   Peng Y K M and Strickler D J 1986 Features of spherical torus plasmas *Nucl. Fusion*

[3]   Menard J E, Jardin S C, Kaye S M, Kessel C E and Manickam J 1997 Ideal MHD stability limits of low aspect ratio tokamak plasmas *Nucl. Fusion*

[4]   Costley A E 2019 Towards a compact spherical tokamak fusion pilot plant *Philosophical Transactions of the Royal Society A: Mathematical, Physical and Engineering Sciences*

[5]   Wagner F, Becker G, Behringer K, Campbell D, Eberhagen A, Engelhardt W, Fussmann G, Gehre O, Gernhardt J, Gierke G V., Haas G, Huang M, Karger F, Keilhacker M, KÏber O, Kornherr M, Lackner K, Lisitano G, Lister G G, Mayer H M, Meisel D, M̈ller E R, Murmann H, Niedermeyer H, Poschenrieder W, Rapp H, Röhr H, Schneider F, Siller G, Speth E, Stäbler A, Steuer K H, Venus G, Vollmer O and Ÿ Z 1982 Regime of improved confinement and high beta in neutral-beam-heated divertor discharges of the ASDEX tokamak *Phys. Rev. Lett.* **49** 1408–12

[6]   Kinsey J E, Staebler G M, Candy J, Waltz R E and Budny R V. 2011 ITER predictions using the GYRO verified and experimentally validated trapped gyro-Landau fluid transport model *Nucl. Fusion*

[7]   Zohm H 1996 Edge localized modes (ELMs) *Plasma Phys. Control. Fusion* **38** 105–28

[8]   Leonard A W 2014 Edge-localized-modes in tokamaksa) *Phys. Plasmas* **21** 090501

[9]   Snyder P B, Wilson H R, Ferron J R, Lao L L, Leonard A W, Osborne T H, Turnbull A D, Mossessian D, Murakami M and Xu X Q 2002 Edge localized modes and the pedestal: A model based on coupled peeling-ballooning modes *Physics of Plasmas* vol 9 pp 2037–43

[10]   Sykes A, Akers R J, Appel L C, Arends E R, Carolan P G, Conway N J, Counsell G F, Cunningham G, Dnestrovskij A, Dnestrovskij Y N, Field A R, Fielding S J, Gryaznevich M P, Korsholm S, Laird E, Martin R, Nightingale M P S, Roach C M, Tournianski M R, Walsh M J, Warrick C D, Wilson H R and You S 2001 First results from MAST *Nucl. Fusion*

[11]   Saarelma S, Hender T C, Kirk A, Meyer H and Wilson H R 2007 MHD stability analysis of ELMs in MAST *Plasma Phys. Control. Fusion*

[12]   Dickinson D, Saarelma S, Scannell R, Kirk A, Roach C M and Wilson H R 2011 Towards the construction of a model to describe the inter-ELM evolution of the pedestal on MAST *Plasma Phys. Control. Fusion*

[13]   Kirk A, O'Gorman T, Saarelma S, Scannell R and Wilson H R 2009 A comparison of H-mode pedestal characteristics in MAST as a function of magnetic configuration and ELM type *Plasma Phys. Control. Fusion*

[14]   Ono M, Bell M G, Bell R E, Bigelow T, Bitter M, Blanchard W, Darrow D S, Fredrickson E D, Gates D A, Grisham L R, Hosea J C, Johnson D W, Kaita R, Kaye S M, Kubota S, Kugel H W, LeBlanc B P, Maingi R, Maqueda R, Mazzucato E, Menard J, Mueller D, Nelson B A, Neumeyer C, Paoletti F, Paul S F, Peng Y K M, Ramakrishnan S, Raman R, Ryan P M, Sabbagh S A, Skinner C H, Stevenson T, Stutman D, Swain D W, Synakowski E J, Taylor G, Von Halle A, Wilgen J, Williams M, Wilson J R, Zweben S J, Ackers R, Barry R E, Bers A, Bialek J M, Bonoli P T, Carter M D, Chrzanowski J, Davis W, Doyle E J, Dudek L, Efthimion P C, Ellis R, Ferron J R, Finkenthal M, Fredd E, Gibney T, Goldston R J, Hatcher R E, Hawryluck R J, Hayashiya H, Hill K W, Jarboe T R, Jardin S C, Ji H, Kalish M, LaMarche P, Lao L L, Lee K C, Levinton F M, Luhmann N C, Majeski R, Manickam J, Marsala R, Mau T K, McCormack B, Medley S S, Menon M M, Mitarai O, Nagata M, Nishino N, Oliaro G, Park H K, Parsells R, Pearson G, Peebles T, Phillips C K, Pinsker R, Porter G D, Ram A K, Robinson J, Roney P, Roquemore A L, Rosenberg A, Schaffer M, Shiraiwa S, Sichta P, et al 2001 Overview of the initial NSTX experimental results *Nucl. Fusion*

[15]   Diallo A, Canik J, Göerler T, Ku S H, Kramer G J, Osborne T, Snyder P, Smith D R, Guttenfelder W, Bell R E, Boyle D P, Chang C S, Leblanc B P, Maingi R, Podestà M and Sabbagh S 2013 Progress in characterization of the pedestal stability and turbulence during the edge-localized-mode cycle on National Spherical Torus Experiment *Nucl. Fusion*

[16]   Sontag A C, Canik J M, Maingi R, Manickam J, Snyder P B, Bell R E, Gerhardt S P, Kubota S, LeBlanc B P, Mueller D, Osborne T H and Tritz K L 2011 Pedestal characterization and stability of small-ELM regimes in NSTX *Nucl. Fusion*

[17]   Maingi R, Osborne T H, Leblanc B P, Bell R E, Manickam J, Snyder P B, Menard J E, Mansfield D K, Kugel H W, Kaita R, Gerhardt S P, Sabbagh S A and Kelly F A 2009 Edge-localized-mode suppression through density-profile modification with lithium-wall coatings in the national spherical torus experiment *Phys. Rev. Lett.*

[18]   Harrison J R, Akers R J, Allan S Y, Allcock J S, Allen J O, Appel L, Barnes M, Ben Ayed N, Boeglin W, Bowman C, Bradley J, Browning P, Bryant P, Carr M, Cecconello M, Challis C D, Chapman S, Chapman I T, Colyer G J, Conroy S, Conway N J, Cox M, Cunningham G, Dendy R

O, Dorland W, Dudson B D, Easy L, Elmore S D, Farley T, Feng X, Field A R, Fil A, Fishpool G M, Fitzgerald M, Flesch K, Fox M F J, Frerichs H, Gadgil S, Gahle D, Garzotti L, Ghim Y C, Gibson S, Gibson K J, Hall S, Ham C, Heiberg N, Henderson S S, Highcock E, Hnat B, Howard J, Huang J, Irvine S W A, Jacobsen A S, Jones O, Katramados I, Keeling D, Kirk A, Klimek I, Kogan L, Leland J, Lipschultz B, Lloyd B, Lovell J, Madsen B, Marshall O, Martin R, McArdle G, McClements K, McMillan B, Meakins A, Meyer H F, Militello F, Milnes J, Mordijck S, Morris A W, Moulton D, Muir D, Mukhi K, Murphy-Sugrue S, Myatra O, Naylor G, Naylor P, Newton S L, O'Gorman T, Omotani J, O'Mullane M G, Orchard S, Pamela S J P, Pangione L, Parra F, Perez R V., Piron L, Price M, Reinke M L, Riva F, Roach C M, Robb D, Ryan D, et al 2019 Overview of new MAST physics in anticipation of first results from MAST Upgrade *Nucl. Fusion*

[19]   Luxon J L 2002 A design retrospective of the DIII-D tokamak *Nucl. Fusion*

[20]   Walsh M J, Arends E R, Carolan P G, Dunstan M R, Forrest M J, Nielsen S K and O'Gorman R 2003 Combined visible and infrared Thomson scattering on the MAST experiment *Review of Scientific Instruments*

[21]   Scannell R, Walsh M J, Carolan P G, Conway N J, Darke A C, Dunstan M R, Hare D and Prunty S L 2006 Enhanced edge Thomson scattering on MAST *Review of Scientific Instruments*

[22]   Conway N J, Carolan P G, McCone J, Walsh M J and Wisse M 2006 High-throughput charge exchange recombination spectroscopy system on MAST *Review of Scientific Instruments*

[23]   Stammers K and Loughlin M J 2006 The calibration of the MAST neutron yield monitors *Nucl. Instruments Methods Phys. Res. Sect. A Accel. Spectrometers, Detect. Assoc. Equip.*

[24]   Groebner R J and Osborne T H 1998 Scaling studies of the high mode pedestal *Phys. Plasmas*

[25]   Hawryluk R J 1981 AN EMPIRICAL APPROACH TO TOKAMAK TRANSPORT *Physics of Plasmas Close to Thermonuclear Conditions* pp 19–46

[26]   Breslau, Joshua and Gorelenkova, Marina and Poli, Francesca and Sachdev, Jai and Yuan X and U O of S 2018 TRANSP *misc* **6**

[27]   Lao L L, John H S, Stambaugh R D, Kellman A G and Pfeiffer W 1985 Reconstruction of current profile parameters and plasma shapes in tokamaks *Nucl. Fusion* **25** 1611–22

[28]   Sauter O, Angioni C and Lin-Liu Y R 1999 Neoclassical conductivity and bootstrap current formulas for general axisymmetric equilibria and arbitrary collisionality regime *Phys. Plasmas* **6** 2834–9

[29]   Miller R L, Chu M S, Greene J M, Lin-Liu Y R and Waltz R E 1998 Noncircular, finite aspect ratio, local equilibrium model *Phys. Plasmas* **5** 973–8

[30]   Connor J W, Hastie R J and Taylor J B 1978 Shear, periodicity, and plasma ballooning modes *Phys. Rev. Lett.*

[31]   Candy J, Belli E A and Bravenec R V. 2016 A high-accuracy Eulerian gyrokinetic solver for collisional plasmas *J. Comput. Phys.*

[32]   Belli E A and Candy J 2018 Impact of centrifugal drifts on ion turbulent transport *Phys. Plasmas*

[33]   Dickinson D, Roach C M, Saarelma S, Scannell R, Kirk A and Wilson H R 2012 Kinetic instabilities that limit β in the edge of a tokamak plasma: A picture of an H-mode pedestal *Phys. Rev. Lett.*

[34] Beurskens M N A, Osborne T H, Schneider P A, Wolfrum E, Frassinetti L, Groebner R, Lomas P, Nunes I, Saarelma S, Scannell R, Snyder P B, Zarzoso D, Balboa I, Bray B, Brix M, Flanagan J, Giroud C, Giovannozzi E, Kempenaars M, Loarte A, De La Luna E, Maddison G, Maggi C F, McDonald D, Pasqualotto R, Saibene G, Sartori R, Solano E, Walsh M and Zabeo L 2011 H-mode pedestal scaling in DIII-D, ASDEX upgrade, and JET *Phys. Plasmas*

[35] Miller R L, Lin-Liu Y R, Turnbull A D, Chan V S, Pearlstein L D, Sauter O and Villard L 1997 Stable equilibria for bootstrap-current-driven low aspect ratio tokamaks *Phys. Plasmas*

[36] Snyder P B, Hughes J W, Osborne T H, Paz-Soldan C, Solomon W M, Knolker M, Eldon D, Evans T, Golfinopoulos T, Grierson B A, Groebner R J, Hubbard A E, Kolemen E, LaBombard B, Laggner F M, Meneghini O, Mordijck S, Petrie T, Scott S, Wang H Q, Wilson H R and Zhu Y B 2019 High fusion performance in Super H-mode experiments on Alcator C-Mod and DIII-D *Nucl. Fusion* **59** 086017

[37] Lortz D 1975 The General "Peeling" Instability *Nucl. Fusion* **15** 49–54

[38] Wesson J A 1978 Hydromagnetic stability of tokamaks *Nucl. Fusion* **18** 87–132

[39] Connor J W, Hastie R J, Wilson H R and Miller R L 1998 Magnetohydrodynamic stability of tokamak edge plasmas *Phys. Plasmas*

[40] Connor J W 1998 A review of models for ELMs *Plasma Phys. Control. Fusion* **40** 191–213

[41] Cooper A 1992 Variational formulation of the linear MHD stability of 3D plasmas with noninteracting hot electrons *Plasma Phys. Control. Fusion* **34** 1011–36

[42] Knolker M, Bortolon A, Canal G P, Evans T E, Zohm H, Abrams T, Buttery R J, Davis E M, Groebner R J, Hollmann E, Fenstermacher M E, Lasnier C, Leonard A W, Moyer R A, Nazikian R, Osborne T H, Paz-Soldan C and Sieglin B 2018 Investigation of the role of pedestal pressure and collisionality on type-I ELM divertor heat loads in DIII-D *Nucl. Fusion* **58** 096023

[43] Snyder P B, Groebner R J, Hughes J W, Osborne T H, Beurskens M, Leonard A W, Wilson H R and Xu X Q 2011 A first-principles predictive model of the pedestal height and width: Development, testing and ITER optimization with the EPED model *Nucl. Fusion* **51**

[44] Meneghini O, Smith S P, Lao L L, Izacard O, Ren Q, Park J M, Candy J, Wang Z, Luna C J, Izzo V A, Grierson B A, Snyder P B, Holland C, Penna J, Lu G, Raum P, McCubbin A, Orlov D M, Belli E A, Ferraro N M, Prater R, Osborne T H, Turnbull A D and Staebler G M 2015 Integrated modeling applications for tokamak experiments with OMFIT *Nucl. Fusion* **55**